Journal of Applied Fluid Mechanics, Vol. 15, No. 6, pp. 1837-1850, 2022.
Available online at www.jafmonline.net, ISSN 1735-3572, EISSN 1735-3645.
https://doi.org/10.47176/jafm.15.06.1279

Gas-Solid Erosion Study of Elbow Pipe based on Erosion Dynamic Grid Technology

D. S. Zhu, Q. Q. Li†, G. F. Ou, M. H. Luo and Y. J. Gu

School of Mechanical Engineering &Rail Transit, Changzhou University, Changzhou, Jiangsu, 213164, China

†*Corresponding Author Email: 20085700106@cczu.edu.cn*

(Received May 1, 2022; accepted August 1, 2022)

ABSTRACT

The dynamic erosion characteristics of pipe bends exposed to gas-solid two-phase flow are investigated by using an erosion-coupled dynamic meshing method to elucidate the erosion failure phenomenon that is common in pipe elbows, transporting coal fly ash and subjected to particle erosion. The static mesh is compared with the erosion-coupled dynamic mesh method by CFD. The dynamic erosion characteristics of bends with different *r/D* ratios, *D* and *r* are investigated before and after surface deformation under gas-solid two-phase flow. The results lead to the following conclusions: Improved performance of the erosion-coupled dynamic mesh by taking full consideration of the coupling between the erosion-induced surface deformation and the particle motion under prolonged erosion. The erosion rate at the elbow changes significantly upon surface deformation, and the sites with a high risk of erosion shift downstream. With increasing of deformation, the larger the *r/D* ratio, the more obvious the concentration of erosion location evolving downstream. As *D* decreases, the high-risk erosion areas become more concentrated. In particular, the emergence of the "bending increase" phenomenon leads to a different perception of how *r/D* ratio and the diameter affect erosion in static-grid simulations: a larger *r/D* ratio of the elbow makes it more sensitive to surface deformation and increases the erosion rate. This study leads us to consider the coupled deformation of erosion in the context of erosion problems, which has important implications for predicting the service life of overflow components.

Keywords: Elbow; Gas-solid erosion; Erosion-coupled dynamic grid; Numerical simulation; Surface deformation.

1. INTRODUCTION

Pipelines are a major overflow component in the petrochemical and natural gas industries and suffer from surface degradation and even deformation and leakage due to the impact of entrained solid particles on the inner wall of the pipeline when transporting fluids (Wang *et al*. 2020). As an important part of the pipeline system, elbows change the flow direction of the fluid, so erosion problems become more serious than straight pipes (Edwards *et al*. 2001).

A great deal of research has focused on pipeline elbows. For example, Sedrez and Shirazi (2021) investigated the erosion rates in a series of pipe bends under liquid-solid and gas-liquid-solid conditions by combining experimentation and simulations and evaluated how gravity and bend orientation affect erosion under different conditions. The results show that the erosion risk is greater in the second elbow than in the first elbow and that the elbow direction with respect to gravity has a great effect on the erosion rate. Bilal *et al*. (2021) verified their numerical simulation results via elbow paint removal experiments, which they used to study 90° elbows with radius-to-diameter ratios *r/D* = 1.5, 2.5 and 5 and 45° elbows with a radius of curvature of 1.5 *D*. The results show that the erosion rate of the 90° elbow decreases with increasing *r/D*. The erosion rate in a 45° elbow is significantly less than in a 90° elbow. Wang and Yu (2019) considered how applied stress affects erosion and proposed an erosion equation and a numerical simulation method based on test data and the E/CRC erosion equation. Asgharpour and Zahedi (2018) investigated the magnitude and pattern of erosion of two standard continuous vertical-horizontal and horizontal-vertical elbows in gas-sand and gas-liquid-sand annular flows using ultrasonic techniques and paint-removal experiments. The results show that the maximum erosion sites in the first and second elbow occur at about 45° and 65° from the elbow inlet, respectively. In addition, the results show that two high-frequency impact regions in the elbow are mainly due to the first impact of the particles and the rebound after the first impact, respectively. Zolfagharnasab and Salimi (2020) used numerical simulations to study the erosion pattern in square pipes. The results show that the erosion depends

more on the surface area than on the hydraulic diameter and that erosion in square pipes is less affected by flow rate and particle size than in round pipes, which have a greater resistance to erosion. Xu *et al*. (2021) proposed an arc-shaped diversion erosion-inhibiting plate structure, which not only reduces the elbow erosion rate but also improves the elbow flow field and reduces the elbow pressure drop, turbulent kinetic energy, and turbulent dissipation rate. Zhang and Zhang (2021) used numerical simulations to investigate the erosion wear characteristics of bends with corrosion defects. The results of the study show that erosion in the elbow is aggravated when the elbow contains defective areas. In particular, when the defective area is at 55° with respect to the elbow, the erosion rate is maximal. They also studied the structural dimensions of the defective area and found that the size of the defective area affects the erosion area and thus the erosion rate. Zamani and Seddighi (2017) used numerical methods to investigate how particle rotation affects erosion in gas-solid bends. The results show that particle rotation considerably affects the erosion rate and particle trajectory.

Nowadays, most elbow-erosion studies consider only erosion in elbows without erosion defects, which means that they do not consider coupling between (1) the deformation of the inner surface of the elbow due to particle impact and (2) the flow and particle motion fields. With the development of computational fluid dynamics (CFD), the erosion-coupled dynamic mesh technique has become available for predicting how erosion rate varies with surface deformation (ANSYS, ANSYS 2021 R1 Theory Guide. 2021). Adedeji and Duarte (2020) investigated the surface deformation of a standard 90° elbow under different wall conditions using an erosion-coupled dynamic mesh method and verified the numerical results by comparison with experimental data. The results show that the dynamic mesh produces more accurate predictions than the static mesh, and the wall roughness and particle rotation both affect the shape and size of the surface deformation. The results also show that the erosion-coupled dynamic grid method couples the flow and particle motion fields and that the erosion morphology evolves over time, which should allow us to solve more complex erosion problems than is possible with static-grid erosion calculations. Parsi and Jatale (2019) used an erosion-coupled dynamic grid method to numerically investigate how surface deformation affects erosion in impact jet experiments. The results better reproduce the experimental results, demonstrating the superior performance of the method. Duarte and Souza (2020) applied the dynamic freezing flow technique to the erosion-coupled dynamic grid method, which significantly reduces CPU time and allows faster and more accurate prediction of erosion deformation. Sokmen and Karatsa (2020) considered the deformation of air hoses under pressure. The results are more realistic and reliable.

To date, erosion-coupled dynamic mesh methods have mostly been applied to study the deformation of bends, whereas the surface deformation of bends as a function of various factors (*D*, radius of curvature, *r/D* ratios, particle size, fluid properties) has been less studied. The present study thus uses CFD and the experimental data from Vieira and Mansour (2016) to investigate the erosion characteristics of bent pipe under gas-solid conditions. In comparison with static grids, erosion-coupled dynamic grids provide better performance in terms of erosion rate prediction accuracy. The surface deformation of 90° bends as a function of diameter, radius of curvature and *r/D* ratio is investigated by using the erosion-coupled dynamic mesh method to investigate how the flow field and particle motion field depend on deformation. This research provides guidance for accurately predicting the risk of erosion of overflow pipeline components, which helps to accurately predict the service life of pipeline bends.

2. NUMERICAL MODEL

2.1. Model of Gas Phase

The conservation-of-mass and momentum equations for fluid in a pipe undergoing gas-solid two-phase flow are

$$\frac{\partial \rho}{\partial t}+\nabla\cdot\left(\rho\vec{v}\right)=0 \tag{1}$$

$$\frac{\partial}{\partial t}\left(\rho\vec{v}\right)+\nabla\cdot\left(\rho\vec{v}\vec{v}\right)= -\nabla p+\nabla\cdot\left(\bar{\bar{\tau}}\right)+\rho\vec{g}+\vec{F} \tag{2}$$

where p is the static pressure, $\bar{\bar{\tau}}$ is the stress tensor, $\rho\vec{g}$ is the gravitational force, and $\vec{F}$ is the external the force and other model-dependent source terms.

Given the coupling between surface deformation and flow field, we use the Reynolds stress model, which requires seven additional transport equations to describe three-dimensional flow and accounts for flow curvature, vortices, and rapid changes in rotation in a more rigorous manner than is possible with single- and two-equation models, thereby providing more accurate predictions of complex flows. In addition, to obtain highly accurate near-wall computations without degrading the accuracy of the wall mesh, we use the wall-enhancement function (ANSYS, ANSYS 2021 R1 Theory Guide. 2021).

2.2. Discrete solid particle phase

The discrete phase is treated in a Lagrangian framework, where the fluid is considered a continuum by solving the Navier-Stokes equations. The particle trajectories are then obtained by tracking based on Newton's second law. Since particle rotation is not considered, we do not consider conservation of angular momentum so the trajectory of the particle and the force balance equations are

$$\frac{dx}{dt}=u_p \tag{3}$$

$$m_p \frac{d\vec{u}_p}{dt} = m_p \frac{\vec{u} - \vec{u}_p}{\tau_r} + m_p \frac{\vec{g}\left(\rho_p - \rho\right)}{\rho_p} + \vec{F} \quad (4)$$

where $\vec{u}_p$ is the particle velocity, m_p is the particle mass, $\vec{u}$ is the fluid velocity, ρ is the fluid density, ρ_p is the particle density, $\vec{F}$ is the sum of Saffman lift, virtual mass force, pressure gradient force, Magnus lift, and other additional forces. The Saffman lift is important only for low Reynolds number and submicron particles and is therefore negligible in the present case. The virtual mass force and pressure gradient force are only considered when the fluid density exceeds the particle density, so they can also be neglected. τ_r is the particle relaxation time, and is given by

$$\tau_r = \frac{\rho_p d_p^{\,2}}{18\mu} \frac{24}{C_d \,\mathrm{Re}_p} \quad (5)$$

where μ is the molecular viscosity of the fluid, d_p is the particle diameter, C_D is the drag coefficient, and Re_p is the particle Reynolds number given by

$$\mathrm{Re}_p = \frac{\rho_f d_p \left|\vec{u}_p - \vec{u}\right|}{\mu} \quad (6)$$

The drag coefficients used in the simulations are those of Morsi and Shirazi (1972):

$$C_D = a_1 + \frac{a_2}{\mathrm{Re}_p} + \frac{a_3}{\mathrm{Re}_p^{\,2}} \quad (7)$$

where a_1 , a_2 ,and a_3 are constants drag coefficients whose values depend on the particle Reynolds number, (see Table 1).

Table 1 Drag coefficients

Re_p range	a_1	a_2	a_3
Re_p<0.1	0	24	0
0.1<Re_p<1	3.690	22.73	0.0903
1<Re_p<10	1.222	29.1667	-3.8889
10<Re_p<100	0.6167	46.50	-116.67
100<Re_p<1000	0.3644	98.33	-2778

2.3. Erosion Modeling

We use the erosion model proposed by Oka and Okamura (2005); Oka and Yoshida (2005) to simulate the erosion of bends. This model accounts for how impact angle, particle velocity, particle size, and the type of pipe material affect pipe erosion. The model is expressed as

$$E(\alpha) = E_{90} f(\alpha) \quad (8)$$

where E_{90} is the erosion rate at an impact angle of 90° and is expressed as

$$E_{90} = 10^{-9} \rho_w K \left(aH_v\right)^{bk_1} \left(\frac{V_p}{V^*}\right)^n \left(\frac{d_p}{d^*}\right)^{k_3} \quad (9)$$

where ρ_w is the density of the target material, a and b are constants related to the load relaxation rate of the target material, d_p is particle size, d^* =326 μm is the reference particle size, V_p is the particle velocity, V^* = 104 m/s is the reference velocity, H_v is the Vickers hardness of the target material in GPa.

The impact angle function is

$$f(\alpha) = (\sin\alpha)^{n_1} \left(1 + H_v (1 - \sin\alpha)\right)^{n_2} \quad (10)$$

which considers both plastic deformation and cutting action as erosion mechanisms, $(\sin\alpha)^{n_1}$ is plastic deformation, and $\left(1 + H_v (1 - \sin\alpha)\right)^{n_2}$ is the cutting action. The constants n, n_1, and n_2 depend on the hardness of the target material and are given by

$$n = 2.3\left(H_v\right)^{0.038} \quad (11)$$

$$n_1 = 0.71\left(H_v\right)^{0.14} \quad (12)$$

$$n_2 = 2.4\left(H_v\right)^{-0.94} \quad (13)$$

This study uses sand particles, and the target material is SS316, so ρ_w = 7990 kg/m^3, H_v = 1.83 GPa, k_3 = 0.19, K = 65, and $\left(aH_v\right)^{bk_1} = \left(H_v\right)^{-0.12}$.

2.4. Particle-Wall Rebound Model

We use the restitution model proposed by Grant and Tabakoff (1975), which assumes that particles impacting the pipe wall is a random process influenced by the particle size and shape and that particles rebound after impact, leading to a loss in particle energy and speed. Such particle rebounds from the wall play an important role in particle tracking, and the normal and tangential recovery coefficients are

$$e_n = 0.993 - 1.76\alpha + 1.56\alpha^2 - 0.49\alpha^3 \quad (14)$$

$$e_t = 0.998 - 1.66\alpha + 2.11\alpha^2 - 0.67\alpha^3 \quad (15)$$

2.5. Erosion Coupled with Dynamic Grid

To predict the erosion rate more accurately, we consider how wall deformation affects the erosion process. The coupling between erosion and surface deformation is vital to accurately predict erosion and is incorporated into the erosion-coupled dynamic grid method. This method combines an erosion rate solver with a dynamic grid model and uses a quasi-steady-state approach, where the solution is first obtained for the flow field, then the particles are tracked for the solution, following which the dynamic grid updates the grid according to the particle erosion rate and time step (ANSYS Fluent Theory Guide, V. 21.1 2021). The mesh deformation of a single face is given by

$$\Delta x_{face} = E \times \Delta t_{MM} / \rho_{wm} \quad (16)$$

where E is the wall erosion rate density, Δt_{MM} is the

grid motion time step, and ρ_{wm} is the density of the wall material.

3. Description Of CFD Model And Method

3.1. Description of Cases

Vieira *et al.* (2016) made ultrasonic measurements at 16 points in a standard elbow of 316 stainless steel and studied the erosion rate as a function of gas velocity, particle diameter, and particle flow masses. To verify the accuracy of the prediction of the present working model for erosion, we use the model used in the experiment of Vieira *et al.* (2016) with an inlet length of 13 *D* and an outlet of 8 *D*. The model diagram appears in Fig. 1. In this study, the effect of *r*, *D* and *r/D* on the erosion of the bend is investigated based on the erosion-coupled dynamic grid, and a total of nine cases are compared. Table 2 lists the values used for *r*, *D*, and *r/D*, which are based on the results of Bourgoyne (1989) and Vieira (2014).

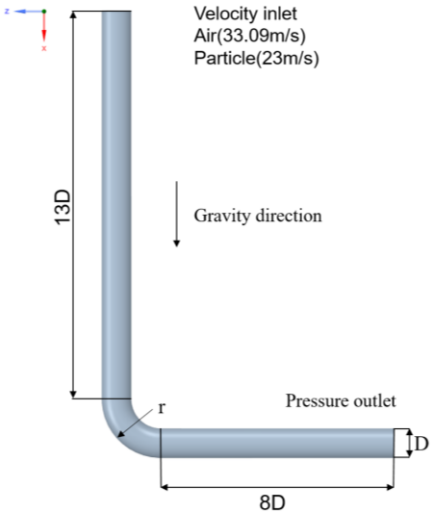

Fig. 1 Geometric schematic.

Table 2 Comparison of bend structure parameters.

Case	*D* (mm)	*r* (mm)	*r/D*
1	76.2	114.3	1.5
2		247.65	3.25
3		381	5
4	50.8	76.2	1.5
5	76.2	114.3	
6	101.6	152.4	
7	50.8	247.65	4.875
8	76.2		3.25
9	101.6		2.4375

3.2. Grid Set-Up

An accurate prediction of the erosion rate depends strongly on the grid-element size. Xie *et al.* (2021) used CFD to investigate how axial and circumferential elbow lengths affect the erosion rate and erosion phenomorphology. The results show that the most accurate prediction is obtained when the axial and circumferential lengths are the same and fall in the range of $10d_p$-$20d_p$. The correlation between the first layer grid thickness (FLT) and the erosion rate at the near-wall surface was investigated by Darihaki *et al.* (2021), who showed that 300 μm particles are not sensitive to the thickness of the first grid layer under gas-solid conditions. Zhang *et al.* (2018) found that, found that, for large particles, errors in particle-impact angle and particle-impact velocity increase upon decreasing the grid thickness of the first near-wall layer, and they suggest using a larger grid spacing for the near-wall layer for large particles. To summarize, the axial and circumferential lengths used in the present simulation are 3 mm, the thickness of the first layer of the mesh is 0.2 mm, and the total number of grid elements is 1.2 million. Fig. 3 shows the mesh.

3.3. Boundary Conditions and Numerical Set-Up

The boundary conditions used for the simulations in this study are the same as those used in all experiments of Vieira *et al.* (2016) (see Fig. 1). The velocity inlet, pressure outlet, fluid, and particle-specific parameters are listed in Table 3. Considering the effect of gravity, the turbulence intensity and hydraulic diameter are 5% and *D*, respectively. The solution uses the SIMPLE coupled pressure-velocity algorithm, the pressure, momentum, and turbulence equations are all of second order, and the flow-field residuals converge to within 1×10^{-8}. The interaction between particles and vortices is modeled by discrete random wandering, all cases track 200 000 particles, and the collision angle and number of particle collisions in particle motion are obtained by UDF. After obtaining the initial erosion rate for the static grid, the erosion-coupled dynamic grid is enabled, and the solution uses a variable time step. Figure 2 shows the results of grid verification: the 1.2 million grid used herein suffices to ensure grid independence.

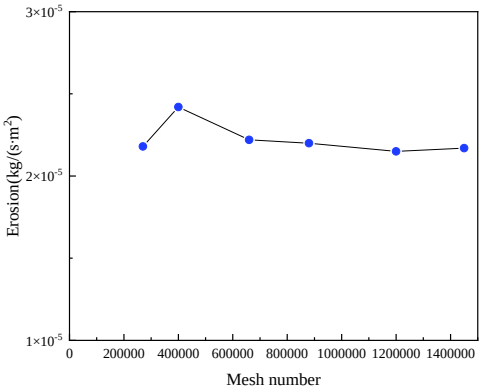

Fig. 2. Grid independence validation.

3.4. Verification of Erosion Model

To verify the suitability of the erosion model and grid settings and to ensure repeatable simulation results, we compare the results produced by the erosion-

Table 3 Air and particle parameters

Air inlet velocity	33.09 m/s
Air density	1.2 kg/m^3
Air viscosity	1.8×10^{-5} kg/(m·s)
Sand inlet velocity	23 m/s
Sand mass flowrate	227 kg/day
Sand density	2650 kg/m^3
Sand size	300μm
Exp.time	45min

coupled dynamic grid after 2700 s simulation time with the experimental results of Vieira and Mansour (2016) for a 90° elbow of 76.2 mm diameter injected with 300-μm-diameter particles. The inconsistency between simulated and experimental fluid velocities is based on the experimental database of 0.7 times the fluid velocity corresponding to the particle velocity (Shirazi *et al*. 1995; McLaury *et al*. 2000; Mazumder *et al*. 2004). The CFD prediction is compared with measurements in Table 4, and the simulation results appear in Fig. 4. The erosion morphology is V-shaped, the maximum erosion rate is converted to mm/yr, the error with respect to the measured results is around 4.98%, and the maximum erosion rate is near 47°, which is consistent with the measured results. Therefore, the erosion model and grid settings are appropriate for subsequent prediction studies.

4. RESULTS AND DISCUSSIONS

4.1. Results Comparison between Static and Dynamic Mesh

In static grid, the coupling between surface deformation and particle movement is not taken into account as erosion time increases, thus its erosion characteristics are independent of the time parameter. However, the erosion-coupled dynamic grid combines the erosion rate solver with dynamic grid model. As the erosion time increases, the dynamic

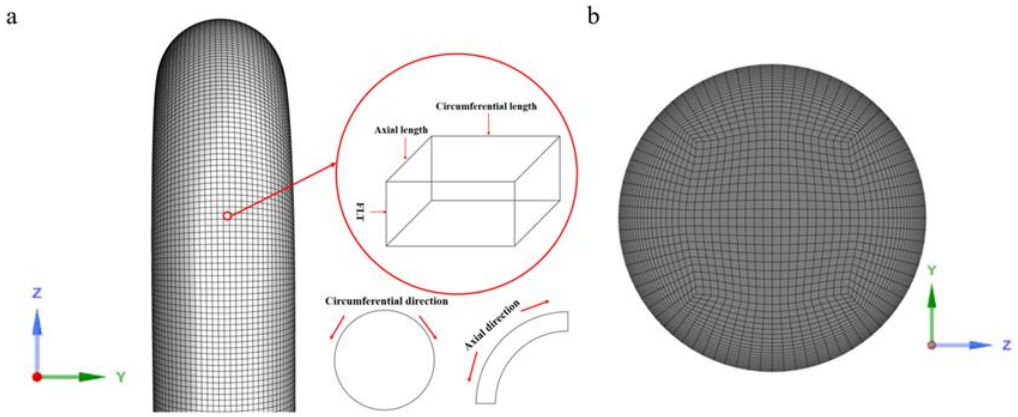

Fig. 3. Grid diagram, (a) elbow side view, (b) elbow inlet.

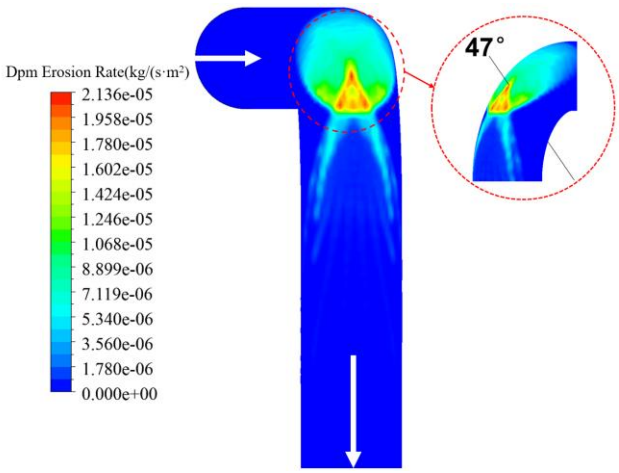

Fig. 4. Erosion contour of the elbow in this study.

Table 4 Comparison of CFD prediction and measurement results

	V_{GAS} (m/s)	Sand Size (μm)	Sand rate (Kg/day)	Erosion rate (mm/yr)	Max erosion location
Exp	23	300	227	80.3	47°
CFD	33.09	300	227	84.3	47°

mesh is capable of gradually expanding to fully capture the coupling between surface deformation and particle motion, where this effect is not distinct during short erosion times.

Figure 5 shows a comparison of the predicted erosion rates for the dynamic grid and the static grid (case 1). The erosion rate predicted by the dynamic grid increases with erosion time, and the longer the erosion time, the greater the increase in erosion rate. The erosion rate predicted by the static grid remains unchanged during the whole erosion time. The duration of the experiment was 45 min, which is also the first data point in Fig. 5(cf. Table 4). For the static grid, the error with the experiment was 5.6%, while the error decreases to 4.98% for the dynamic grid. The erosion rate increases by 23.4% when the erosion time reaches 3×10^6 s. In fact, as the erosion time increases, the erosion area decreases, which is accompanied by an increase in the number of particle impacts. All these phenomena inevitably lead to an increase in erosion rate (e.g. Figs. 25, 26). Therefore, the result of dynamic grid is more accurate and closer to the real erosion rate. Parsi and Jatale (2019) also verified the effect of erosion duration on dynamic grid results.

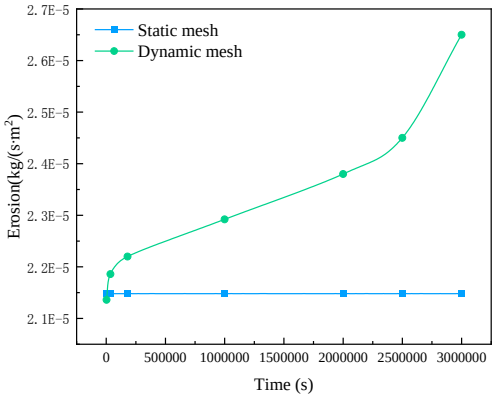

Fig. 5. Comparison of erosion rates for dynamic and static grid.

Figure 6 shows a comparison of the impact angle for the dynamic mesh and the static mesh simulation (case 7). The maximum angle of impact at the static grid elbow is 27.9°, at 33° in the elbow. The results of the dynamic grid at 10^6 s are similar to the static grid results. This indicates that the part is still usable as the pipe has surface deformation but has not yet reached the failure stage. The maximum impact angle of the dynamic grid is 35° under the operation of 2.5×10^6 s, at 37° in the elbow. As the particles continuously impact and move downstream, the position of the deformation on the inner surface of the elbow evolves downstream. This phenomenon was also presented in the studies of Duarte and Souza (2020), Adedeji and Duarte (2020). Compared to static mesh, dynamic mesh can capture changes in impact angle and position due to deformation.

In summary, the performance of the dynamic grid in predicting elbow erosion is better, so the dynamic grid is chosen for the study in this paper. The relationship between the erosion characteristics of the elbow before and after surface deformation on a dynamic grid and *r/D*, *D*, *r* has not yet been investigated. The results will be compared in sections 4.2, 4.3 and 4.4 using erosion-coupled dynamic grid runs at 2700 s versus 10^6 s to investigate the change in erosion characteristics due to deformation.

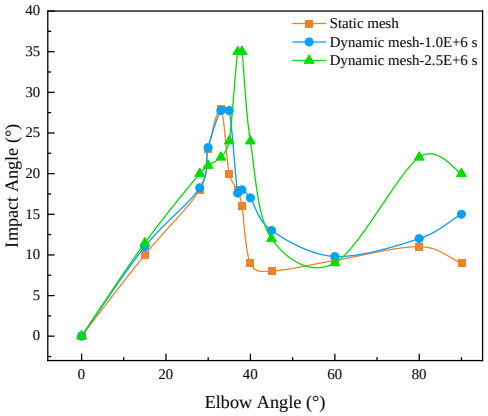

Fig. 6. Comparison of impact angle for dynamic and static grid.

4.2. Effect of different *r/D* ratios on dynamic erosion distribution and particle trajectory in elbows

Figure 7 shows the erosion rates for elbows with a 76.2 mm diameter and different *r*/*D* ratios after 2700 s simulation time (cases 1-3 in Table 2). The erosion rate decreases significantly with increasing *r*/*D* ratio, with a high-risk erosion morphology interval of 45°-60° at *r*/*D* = 1.5, 33°-43.5° at *r*/*D* = 3.25, and 28°-35.5° at *r*/*D* = 5. The high-risk erosion sites gradually shift toward the entrance, and the angular interval decreases significantly with increasing *r*/*D*, but the axial length and erosion area increase later. The maximum erosion area is concentrated at the top of the erosion risk area when *r*/*D* is small, for example, at 45° in the elbow with *r*/*D* = 1.5. At larger *r*/*D*, the maximum erosion is concentrated at the bottom of the erosion risk area over a significantly larger area, for example, at 43.5° in the elbow with *r*/*D* = 3.25. Figures 8-10 show the flow field and particle motion field characteristics of the elbow at different *r*/*D* ratios. As *r*/*D* increases, the flow field changes more smoothly, the pressure difference at the elbow decreases significantly, and the particle impact number and impact angle also decrease. The position of maximum erosion in Fig. 9(a) corresponds to the maximum number of impacts, whereas the maximum erosion in Figs. 9(b) and 9(c) occurs at the bottom of the high-risk erosion area, which corresponds to the maximum impact angle. This situation occurs because the particle impact angle determines the impact momentum transferred by individual particles to the wall, and the larger impact angle at the bottom of the erosion area makes the total impact momentum of the particles at the bottom greater than at the top when the difference in the number of particle impacts between the top and bottom decreases. A comprehensive analysis shows

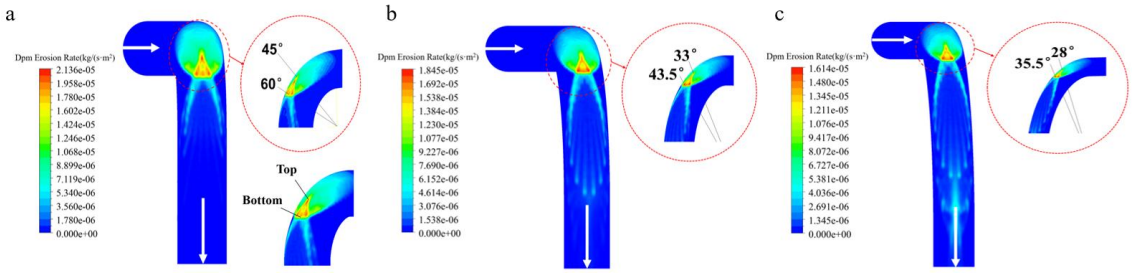

Fig. 7. Erosion rate for elbows with *D*=76.2 mm at 2700 s: (a) 1.5*D*, (b) 3.25*D*, (c) 5*D*.

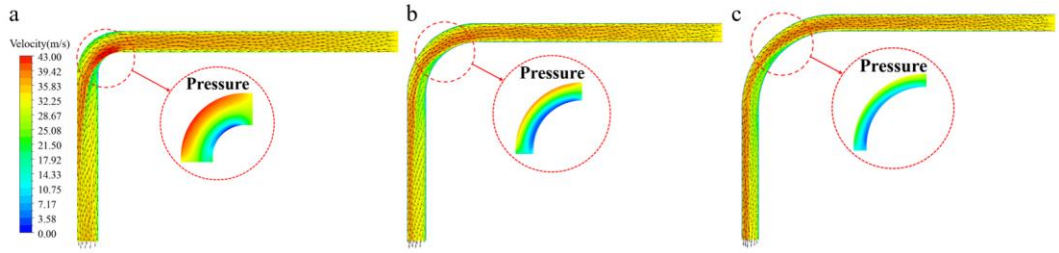

Fig. 8. Flow field characteristics for elbows with *D*=76.2 mm at 2700 s: (a) 1.5*D*, (b) 3.25*D*, (c) 5*D*.

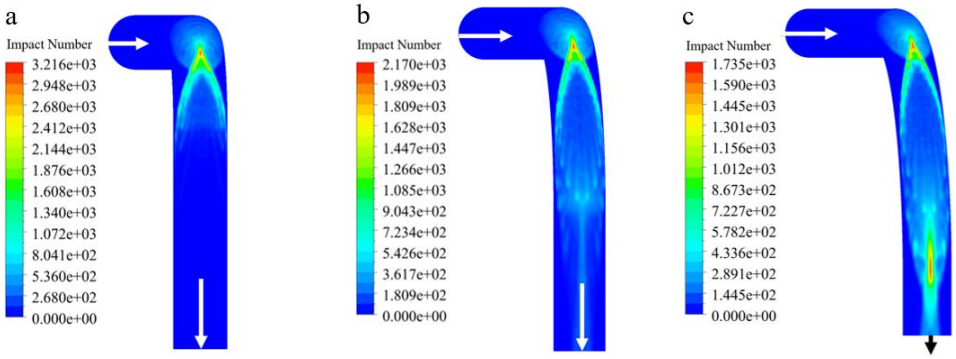

Fig. 9. Number of particle impacts for elbows with *D*=76.2 mm at 2700 s: (a) 1.5*D*, (b) 3.25*D*, (c) 5*D*.

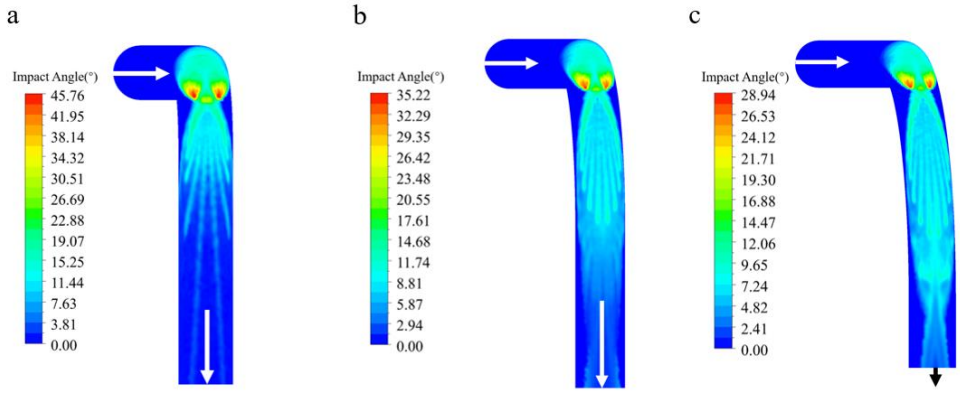

Fig. 10. Impact angle for elbows with *D*=76.2 mm at 2700 s: (a) 1.5*D*, (b) 3.25*D*, (c) 5*D*.

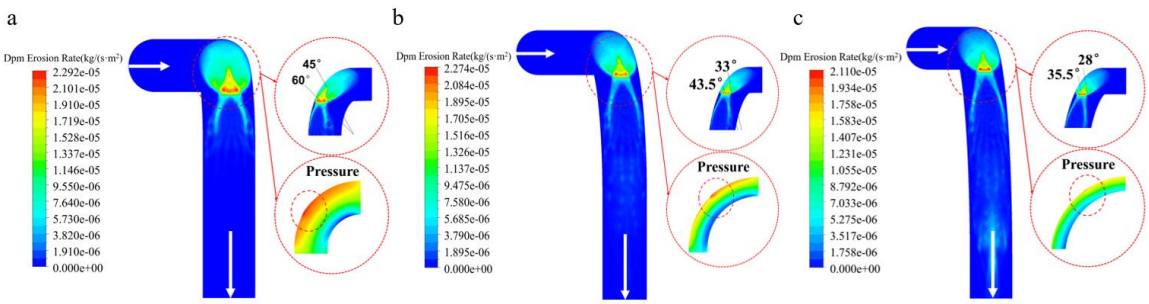

Fig. 11. Erosion rate for elbows with *D*=76.2 mm at 10^6 s: (a) 1.5*D*, (b) 3.25*D*, (c) 5*D*.

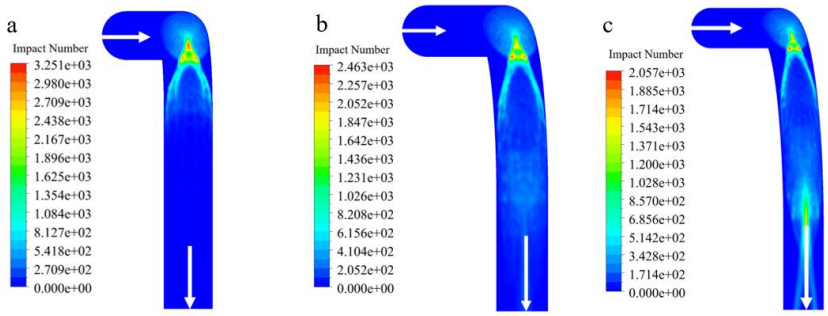

Fig. 12. Number of particle impacts for elbows with *D*=76.2 mm at 10^6 s (a) 1.5*D*, (b) 3.25*D*, (c) 5*D* .

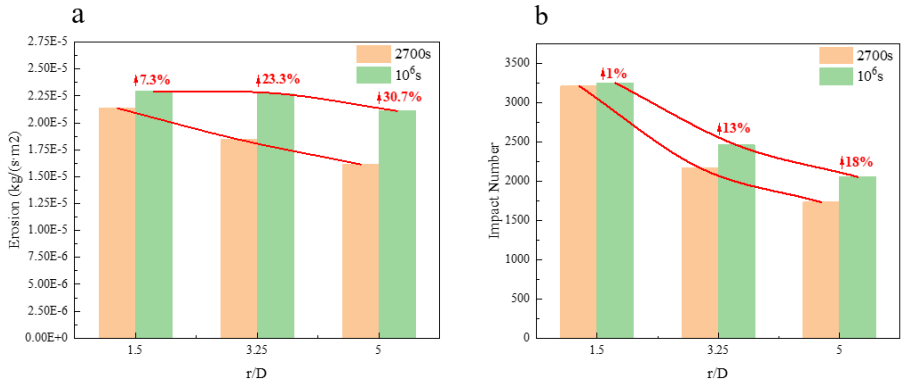

Fig. 13. Effect of *r/D* ratio on erosion rate and particle impact number at different erosion time.

that, as the radius of curvature increases, the erosion rate decreases because a larger radius of curvature translates into a larger *r*/*D*, which in turn means that the flow channel structure is smoother, the impact angle is smaller, the impact momentum is smaller (both normal and tangential), and the erosion area increases so that the number of particles impacting per unit area decreases.

Figures 11 and 12 show the erosion morphology, flow field, and particle motion field of the elbow after 10^6 s simulation time using an erosion-coupled dynamic grid. The erosion rate at the elbow increases significantly, and the high-risk erosion area evolves and concentrates at the bottom, near 60°, 43.5°, and 35.5° in the elbow. The surface deformation is located at the site of pressure concentration, which in turn is due to fluid flow into the elbow and the change in flow direction, leading to a high-pressure, low-velocity area at the wall of the elbow outlet. The surface deformation creates discontinuities in the wall structure of the elbow outlet, leading to pressure concentration in the deformation zone. The number of particle impacts thus increases significantly upon the emergence of smaller surface deformations, which is consistent with the evolution of the erosion morphology, all of which is concentrated near the bottom of the elbow.

In contrast, flow rate and impact angle remain almost the same as before the deformation, which means that the surface deformation is such that the impact angle does not change significantly (cf. Fig. 6). When the deformation is sufficiently large to cause a large change in the impact angle, the pipe must be approaching failure, which is not considered herein. Thus, the change in erosion rate is attributed to the fact that the surface deformation affects the number of particle impacts and the impact area, leading to a greater impact density. Parsi and Jatale (2019) argue that the deformation of the specimen surface changes the particle impact properties and thus the erosion rate, which clearly ignores the change in impact area in the high-risk region. Compared with the previous static grid of erosion morphology, the erosion-coupled dynamic grid produces a more realistic representation of erosion, allowing it to accurately predict the position of high-risk erosion areas.

Figure 13 shows how *r*/*D* affects the dynamic erosion rate and particle impact number at the elbow. At 2700 s simulation time, the erosion rate decreases less for *r*/*D* in the range of 3-5, which is reasonable. Peng (2016) also found that *r*/*D* decreases more slowly in the 3-5 range.

Compared with the erosion rate at 2700 s simulation time, the erosion rate at 10^6 s simulation time increases by 7.3%, 23.3%, and 30.7%, and the number of particle impacts increases by 1%, 13%, and 18%, which means that, when *r*/*D* = 1.5, the elbow is susceptible to erosion at the same time that it is more resistant to deformation and more stable under long time operation.

4.3. Effect of Diameter Parameters on Dynamic Erosion Distribution and Particle Trajectory in Elbows with a Given *r/D* Ratio

Figure 14 shows the erosion rates of elbows with *r*/*D* = 1.5 and different diameters operating on an erosion dynamic grid for 2700 s (cases 4-6 in Table 2). The erosion rate decreases significantly with increasing diameter. The erosion zones of elbows of different diameters are similar, between 45° and 60°, the erosion morphology distributes evenly over the axial

length in high-risk erosion areas.

Figure 15 shows the flow field of elbows of different diameters, which shows that the flow field in these elbows is similar to that in pipes of different diameters but the same *r*/*D* ratio. Figures 16 and 17 show the particle motion field, which shows that the number of particle impacts decreases significantly as the diameter increases, while the impact angles all remain around 45°. Comparing with the results presented in Sec. 4.2 shows that the *r*/*D* ratio is the dominant factor determining the particle impact angle and erosion position at the elbow and that the particle impact angle and erosion position remain basically the same for the same *r*/*D*. Therefore, the erosion rate decreases with diameter because, for a given number of particles and *r*/*D* ratio, the elbow with large diameter generates an erosion domain of larger axial size and circumferential size, leading to more dispersed particle impact. Thus, the erosion area increases, and the number of particle impacts per unit area decreases.

Figure 18 shows the erosion morphology and flow field characteristics of the elbow after 10^6 s simulation time using an erosion-coupled dynamic grid. The erosion rate at the elbow with D = 50.8 mm increases significantly once surface deformation

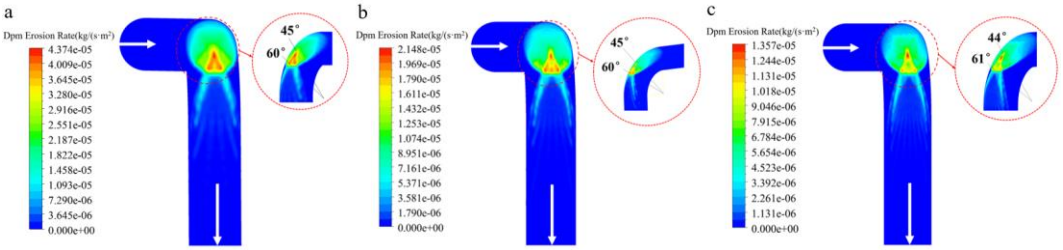

Fig. 14. Erosion rate for elbows with *r/D*=1.5 at 2700 s: (a) 50.8mm, (b) 76.2mm, (c) 101.6mm.

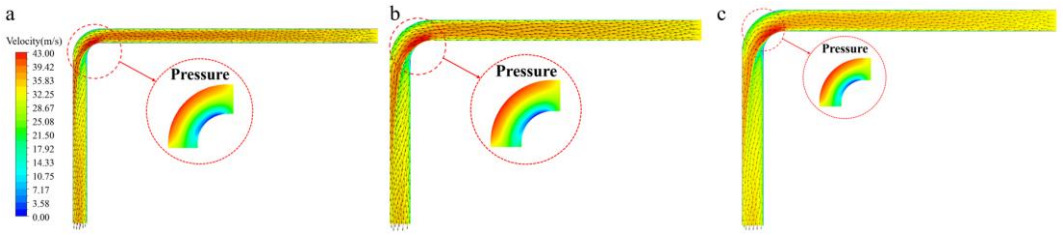

Fig. 15. Flow field characteristics for elbows with *r/D*=1.5 at 2700 s: (a) 50.8mm, (b) 76.2mm, (c) 101.6mm.

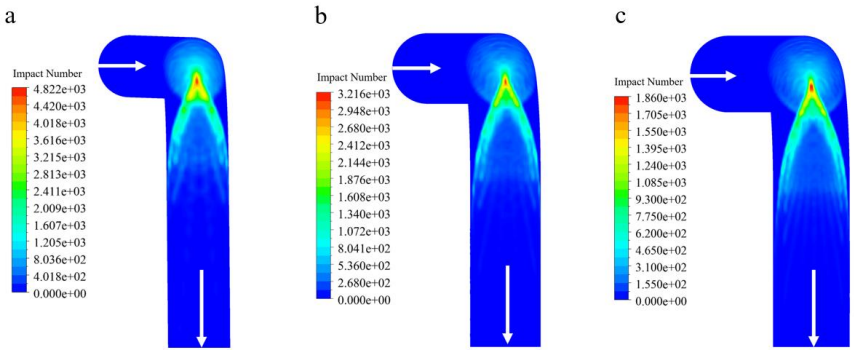

Fig. 16. Number of particle impacts for elbows with *r/D*=1.5 at 2700 s: (a) 50.8mm, (b) 76.2mm, (c) 101.6mm.

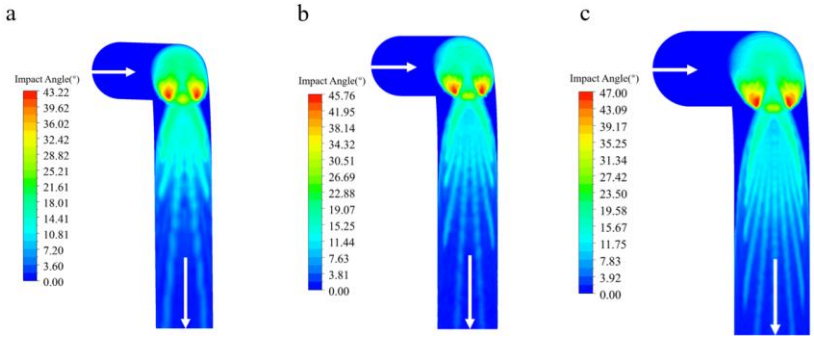

Fig. 17. Impact angle for elbows with *r/D*=1.5 at 2700 s: (a) 50.8mm, (b) 76.2mm, (c) 101.6mm.

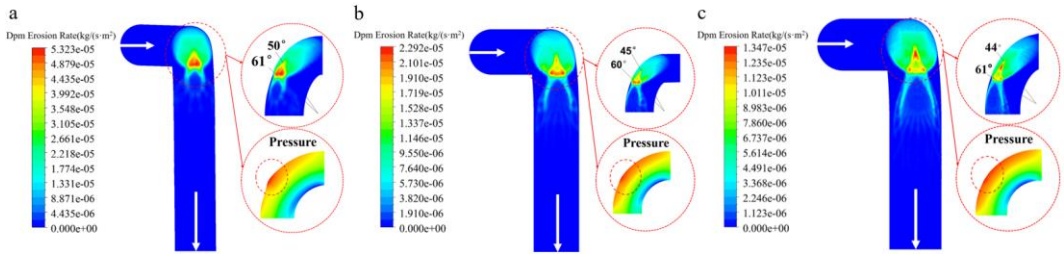

Fig. 18. Erosion rate for elbows with *r/D*=1.5 at 10^6 s: (a) 50.8mm, (b) 76.2mm, (c) 101.6mm.

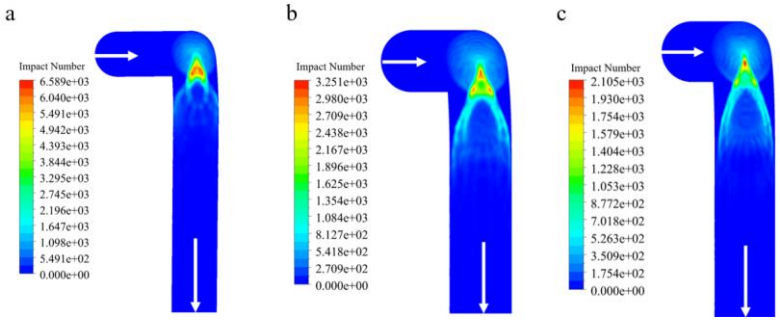

Fig. 19. Number of particle impacts for elbows with *r/D*=1.5 at 10^6 s: (a) 50.8mm, (b) 76.2mm, (c) 101.6mm.

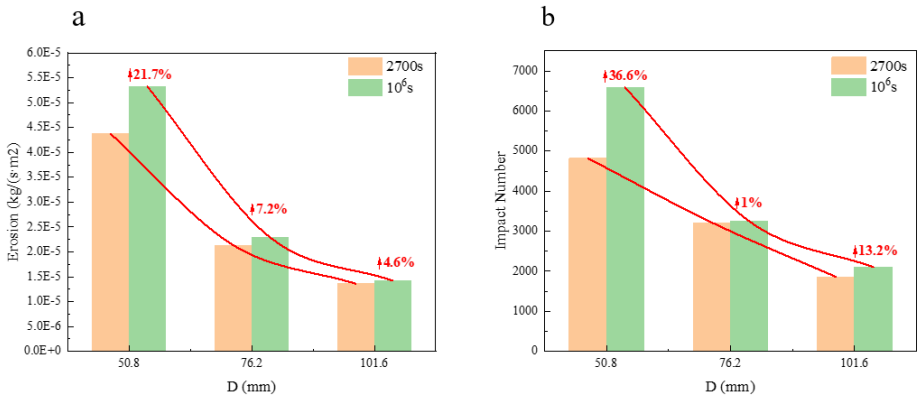

Fig. 20. Effect of *D* on erosion rate and particle impact number of elbows with *r/D*=1.5 at different erosion times.

occurs, whereas the erosion rates at the elbows with D = 76.2 and 101.6 mm remain almost unchanged. This is attributed to the greater resistance of the elbow to deformation at r/D = 1.5, with less erosion variation at smaller deformations. However, the elbow with D = 50.8 mm experiences greater surface deformation, so the erosion rate increases rapidly and the high-risk erosion area shifts from 45°-60° to 50°-61°, the pressure increases in the deformation area, and the erosion evolves and concentrates near the bottom of the high-risk erosion area.

Figure 19 shows the particle motion field after the elbow has eroded for 10^6 s. The large surface deformation leads to a sharp increase in the number of particle impacts, and the impact area and erosion area basically converge. In addition, the axial and circumferential dimensions of the V-shaped erosion morphology in Figs. 18 and 19 decrease. With increasing deformation of the inner surface of the elbow, the particle erosion area becomes concentrated at the deformation, and the erosion area outside the deformation is reduced (cf. Fig. 14).

Figures 20(a) and 20(b) show the variation of erosion rate and the number of impacts as a function of pipe diameter and erosion time. Figure 20(a) shows that, at 2700 s simulation time (i.e., without surface deformation), the erosion rate decreases more for D < 100 mm and less for D > 100 mm. This is consistent with the results of McLaury and Shirazi (2000) and produces a linear relationship between erosion rate and$1/D^2$. Figure 20(b) shows that the number of particle impacts is linear versus $1/D$ at 2700 s. At the erosion simulation time of 10^6 s, the erosion rate increases by 21.7%, 7.2%, and 4.6%, and the number of particle impacts increases by 36.6%, 1%, and 13.2%.

An elbow with D = 101.6 mm shows an unreasonable increase in the number of particle impacts, which is caused by errors and is within the acceptable range. The change in erosion rate and the number of particle impacts at 10^6 s show that the erosion rate at this simulation time is related not only to$1/D^2$ but also to the erosion duration and to the surface deformation, which affects the impact area and the number of particle impacts, making it more difficult to predict the erosion.

4.4. Effect of *D* on Dynamic Erosion Distribution and Particle Trajectory in Elbows with a Fixed Radius of Curvature

Figure 21 shows the erosion rates of elbows with r = 247.65 mm and different diameters simulated with an erosion-coupled dynamic grid for 2700 s (cases 7-9 in Table 2). The erosion rate decreases significantly with increasing diameter, and the erosion interval is 27.5°-36° for D = 50.8 mm, 33°-43.5° for D = 76.2 mm, and 36°-50° for D = 101.6 mm. The erosion distribution is like that obtained in Sec. 4.2: a larger r/D corresponds to a smaller erosion distribution, which appears closer to the elbow entrance. Consider Figs. 21(a)-21(c): the maximum erosion area occupies a larger fraction in Fig. 21(a) than in Figs. 21(b) and 21(c). Figures 22-24 show the flow field and particle motion field in an elbow with r = 247.65 mm and different diameters. As the diameter decreases, r/D increases, the flow field becomes smoother at the elbow, the number of particle impacts increases, and the impact angle decreases.

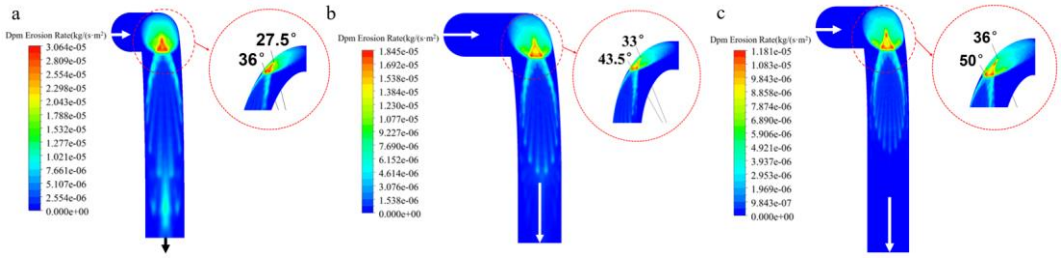

Fig. 21. Erosion rate for elbows with r =247.65mm at 2700 s: (a) 50.8 mm, (b) 76.2 mm, (c) 101.6mm.

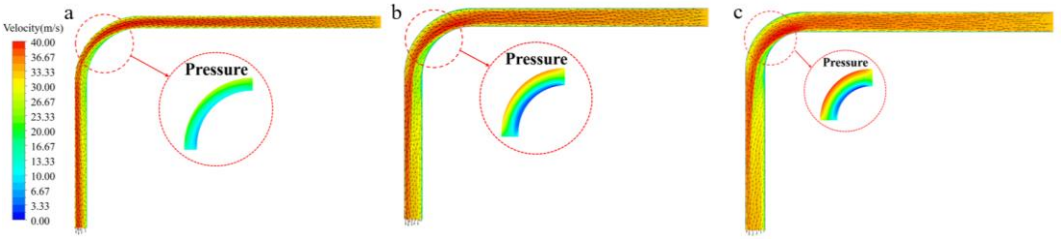

Fig. 22. Flow field characteristics for elbows with r =247.65mm at 2700 s: (a) 50.8 mm, (b) 76.2 mm, (c) 101.6mm.

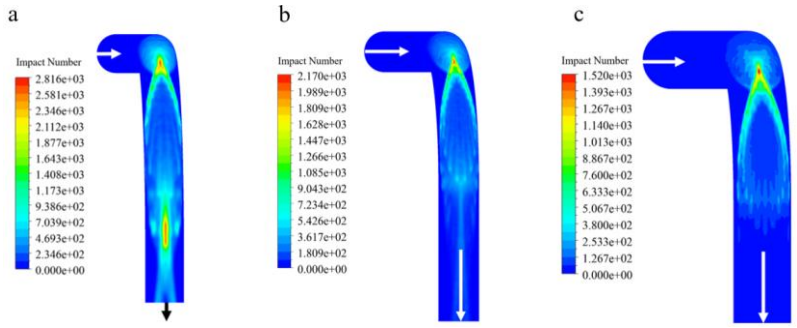

Fig. 23. Number of particle impacts for elbows with r =247.65mm at 2700 s: (a) 50.8mm, (b) 76.2mm, (c) 101.6mm.

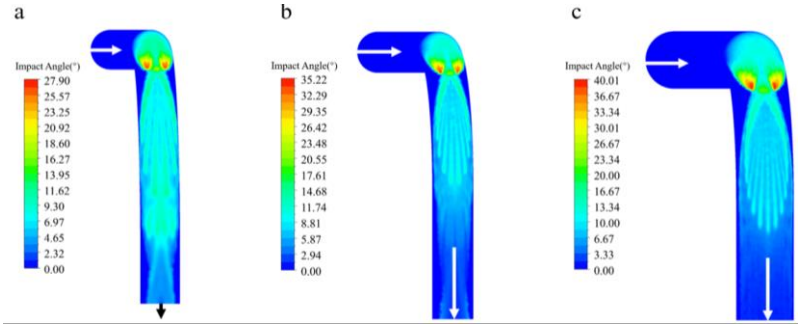

Fig. 24. Particle impact angle for elbows with r =247.65mm at 2700 s: (a) 50.8 mm, (b) 76.2 mm, (c) 101.6mm.

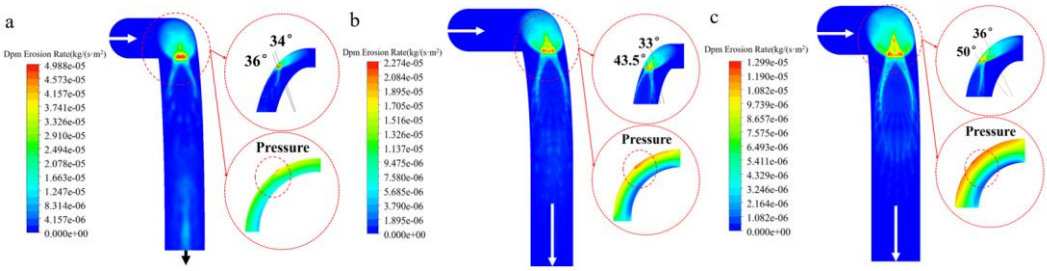

Fig. 25. Erosion rate for elbows with *r* =247.65mm at 10^6 s: (a) 50.8 mm, (b) 76.2 mm, (c) 101.6mm.

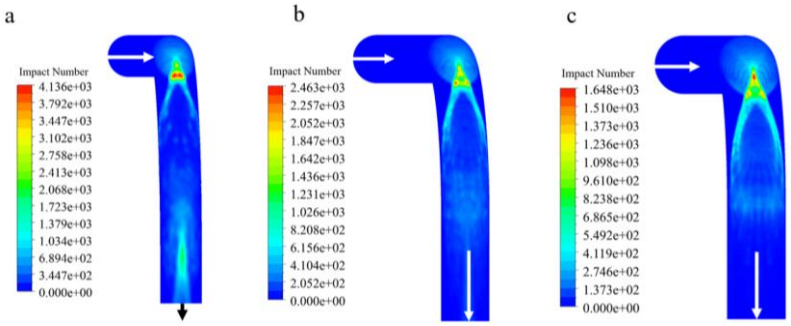

Fig. 26. Number of particle impacts for elbows with *r* =247.65mm at 10^6 s: (a) 50.8mm, (b) 76.2mm, (c) 101.6mm.

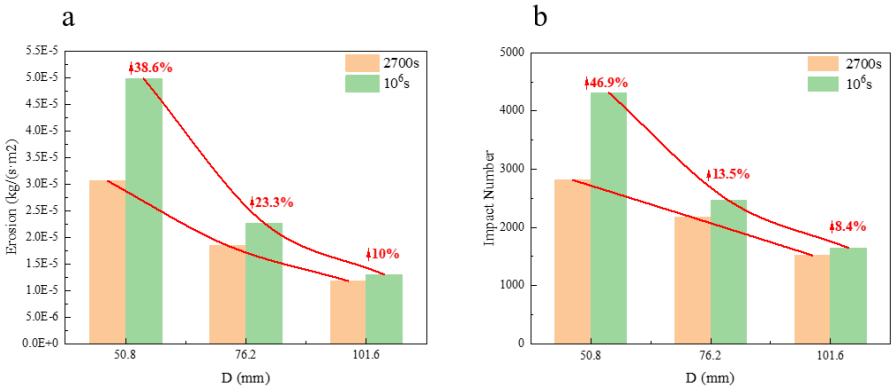

Fig. 27. Effect of *D* on the erosion rate and particle impact number of the elbow with *r*=247.65mm at different erosion times.

Figures 25 and 26 show the erosion morphology, flow field, and particle motion field of the elbow at the simulation time of 10^6 s using the erosion-coupled dynamic mesh. The erosion rate at the elbow increases significantly upon surface deformation, the high-risk erosion area becomes concentrated near the bottom of the elbow, and the pressure increases in the deformed area. Comparing Fig. 11 with Fig. 25 shows that a larger deformation creates a greater concentration of high-risk downstream erosion areas. As in Fig. 25(a), when the elbow undergoes large deformation, its erosion interval shifts to 34°-36°, and the erosion rate and number of particle impacts surge and are concentrated in the deformation area. In addition, the results show that elbows with a larger *r/D* experience slight erosion in their straight sections; for example, two areas of high-frequency particle impact appear in Fig. 23(a). This is because the smooth flow channel translates into less kinetic energy loss of the fluid as it passes through the elbow, and the impact angle and rebound angle decrease as *r*/*D* increases, so the particles collide with the outer wall several times in elbows with larger *r*/*D* (Peng and Cao 2016) and the rebound particles erode the straight pipe section downstream of the elbow. Compared to the erosion morphology of elbows with cases1-9 (see Secs. 4.2, 4.3, and 4.4), the result shows that the erosion area in the straight pipe at a simulation time of 10^6 s decreases significantly, the secondary high-frequency impact area gradually disappears, and the erosion area becomes smaller. This is due to the significant kinetic energy lost in the collisions of most particles at the elbow deformation. This also explains the change in V-shaped erosion morphology. Figure 27 shows how the erosion rate and the number of particle impacts vary with diameter: the number of impacts correlates with 1/*D* at 2700 s simulation time or when no surface deformation occurs. In contrast with the particle impact number at 2700 s in Fig. 20, the growth in the slope decreases because *r*/*D* is also a function of 1/*D* when *r* is constant. After 10^6 s of simulated erosion time and for pipe diameters *D* = 50.8, 76.2, 101.8 mm, the erosion rate increases by 38.6%, 23.3%, and 10%, and the number of particle impacts increases by 46.9%, 13.5%, and 8.4%, respectively.

Compared with the results for D = 50.8 mm in Fig. 20 and combined with the results obtained in Sec. 4.2, the increase in erosion rate at 10^6 s increases significantly with increasing r/D, and a clear "bending increase" phenomenon occurs, which means that a larger the r/D corresponds to the erosion becoming more sensitive to surface deformation. Unlike the results of previous static-grid studies, this "bending increase" phenomenon means that, at a given time, elbows with larger r/D have higher erosion rates than those with smaller r/D, making it more difficult to predict the position of erosion risk. This means that, when surface deformation occurs, a smaller r/D translates into a more stable growth of elbow erosion, facilitating the task of predicting the erosion rate and the location of erosion. This is especially true for longer erosion times or in the case of erosion damage, where the deterioration resistance is superior, but only if the amount of deformation does not significantly change the impact angle.

5. CONCLUSION

In this study, the erosion-coupled dynamic grid method is applied to examine the erosion characteristics of 90° elbows in comparison with static grids. Characteristics parameters such as r/D, D and r are applied to describe the change pattern of erosion distribution and particle trajectory in the elbow before and after surface deformation. There are some conclusions as follows:

(1) The accuracy of the results for the dynamic grid is 0.62% higher than that of the static grid for an experimental time of 45 min. At 3×10^6 s simulation time, the erosion rate of the dynamic grid increased by 23.4%. At 2.5×10^6 s simulation time, the maximum impact angle improved by 7° and the position of the maximum impact angle shifted by 5° downstream. More consideration of the coupling between erosion-induced surface deformation and particle motion makes the dynamic grid simulation results closer to the real erosion rate.

(2) At 2700 s simulation time (i.e., without surface deformation of the pipe), the erosion rate decreases with increasing r/D and diameter. The erosion, particle impact angle, and secondary impact are all related to the r/D ratio. A larger r/D ratio correlates with a smaller interval of erosion angle, and an erosion closer to the elbow entrance (i.e., smaller erosion angles). Smaller particle impact angles increase the likelihood of secondary impacts.

(3) At 10^6 s simulation time or when surface deformation occurs, the erosion rate increases suddenly with increasing r/D and decreasing diameter. The erosion evolves more realistically, with areas of significant erosion becoming concentrated near the pipe deformation and high-pressure points appearing at the deformation. The variations in particle impact number and diameter become irregular, although more data are needed to verify this mathematical model.

(4) When surface deformation occurs, a smaller diameter and larger r/D correlates with larger deformation, and the more likely it is that the "bending increase" phenomenon occurs. As a result, conventional prediction methods have difficulty predicting the erosion rate after surface deformation, whereas the erosion-coupled dynamic grid method remains capable of predicting the service life of the elbow.

(5) Finally, the erosion-coupled dynamic grid can also be used to predict the effects of electrochemical corrosion, flow corrosion, and particle erosion.

REFERENCES

Adedeji, O. E. and C. A. R. Duarte (2020). Prediction of thickness loss in a standard 90° elbow using erosion-coupled dynamic mesh. *Wear* 460-461,203400.

ANSYS, ANSYS 2021 R1 Theory Guide (2021). Technical Report. *ANSYS Fluent Theory Guide*, V. 21.1.

Asgharpour, A. and P. Zahedi (2018). Experimental Investigation of Solid Particle Erosion in Successive Elbows in Gas Dominated Flows. *ASME 2018 5th Joint US-European Fluids Engineering Division Summer Meeting.*

Bilal, F. S., T. A. Sedrez and S. A. Shirazi (2021). Experimental and cfd investigations of 45 and 90 degrees bends and various elbow curvature radii effects on solid particle erosion. *Wear*, 203646.

Bourgoyne, A. T. (1989). Experimental Study of Erosion in Diverter Systems Due to Sand Production. *SPE/IADC Drilling Conference. Society of Petroleum Engineers*.

Darihaki, F. and J. Zhang (2021). The near-wall treatment for solid particle erosion calculations with CFD under gas and liquid flow conditions in elbows. *Advanced Powder Technology* 32(5), 1663-1676.

Duarte, C. A. R. and F. Souza (2020). Dynamic mesh approaches for eroded shape predictions. *Wear* 484-485.

Edwards, J. K., B. S. Mclaury and S. A. Shirazi (2001). Modeling solid particle erosion in elbows and plugged tees. *Journal of Energy Resources Technology*, 123(4), 277-284.

Grant, G. and W. Tabakoff (1975). Erosion prediction in turbomachinery resulting from environmental solid particles. Journal of Aircraft. *J. Aircr.* 12(5), 471-478.

Mazumder, Q. H., S.A. Shirazi and B. S. McLaury (2004). A mechanistic model to predict sand erosion in multiphaseflow in elbows downstream of vertical pipes, *Corrosion* 04662 (2004) 1-15.

Mclaury, B. S. and S. A. Shirazi (2000). An Alternate Method to API RP 14E for Predicting Solids Erosion in Multiphase Flow. *Journal of Energy Resources Technology* 122(3), 115-122.

Morsi, S. A. and A. J. Alexander (1972). An investigation of particle trajectories in two-phase flow systems. *Journal of Fluid Mechanics Digital Archive (JFM)*, 55(2), 193-208.

Oka, Y. I., K. Okamura and T. Yoshida (2005). Practical estimation of erosion damage caused by solid particle impact: Part 1: effects of impact parameters on a predictive equation. *Wear* 259 (1), 95-101.

Oka, Y. I. and T. Yoshida (2005). Practical estimation of erosion damage caused by solid particle impact: Part 2: mechanical properties of materials directly associated with erosion damage. *Wear* 259 (1), 102-109.

Parsi, M., A. Jatale, M. Agrawal and P. Sharma (2019). Effect of surface deformation on erosion prediction. *Wear* 431 57-66.

Peng, W. S. and X. W. Cao (2016). Numerical prediction of erosion distributions and solid particle trajectories in elbows for gas-solid flow. *Journal of Natural Gas Science and Engineering* 30, 455-470.

Peng, W. S. (2016). *Study on the Solid Particle Erosion Mechanism of Pipe Bend for Multiphase Flow*. Ph. D. thesis, China University of Petroleum, Qingdao, China.

Shirazi, S. A., J. R. Shadley, B. S. McLaury and E. F. Rybicki (1995). A procedure to predict solid particle erosion in elbows and tees. *Journal of Pressure Vessel Technology*. 117 45-52.

Sedrez, T. A. and S. A. Shirazi (2021, July). Erosion evaluation of elbows in series with different configurations. *Wear*,476, 203683.

Sokmen, K. F. and O. B. Karatas (2020). Investigation of Air Flow Characteristics in Air Intake Hoses using CFD and Experimental Analysis based on Deformation of Rubber Hose Geometry. *Journal of Applied Fluid Mechanics* 13(3),871-880.

Vieira, R. E. (2014). *Sand erosion model improvement for elbows in gas production, multiphase annular and low-liquid flow.* Dissertations & Theses - Gradworks. The University of Tulsa, Oklahoma, USA.

Vieira, R. E., A. Mansour, B. S. Mclaury and S. A. Shirazi (2016). Experimental and computational study of erosion in elbows due to sand particles in air flow. *Powder Technology* 288, 339-353.

Wang, Q.C., Q. Huang, X. Sun, J. Zhang and S. A. Shirazi (2020). Experimental and numerical evaluation of the effect of particle size on slurry erosion prediction. *Journal of Energy Resources Technology*, 143(7), 1-19.

Wang, H.K., Y. Yu, J. Yu, Z. Wang and H. Li (2019). Development of erosion equation and numerical simulation methods with the consideration of applied stress. *Tribology International*, 137, 387-404.

Xie, Z.Q., X. W. Cao, J. Zhang, F. Darihaki, S. Karimi and N. Xiong and L. Qigui (2021). Effect of cell size on erosion representation and recommended practices in cfd. *Powder Technology*. 389(9), 522-535.

Xu, L. Y., F. Wu., Y. Yan., X. X. Ma and Z. Q. Hui and L. Wei (2021). Numerical simulation of air-solid erosion in elbow with novel arc-shaped diversion erosion-inhibiting plate structure. *Powder Technology*, 393, 670-680.

Zamani, M., S. Seddighi and H. R. Nazif (2017). Erosion of natural gas elbows due to rotating particles in turbulent gas-solid flow. *Journal of Natural Gas Science and Engineering*, 40, 91-113.

Zhang, J., H. Zhang, X. Chen and C. Y. Yu (2021). Gas-solid erosion wear characteristics of elbow pipe with corrosion defects. *Journal of Pressure Vessel Technology*, 143(5).

Zhang, J, B. S. McLaury and S. A. Shirazi (2018). Application and experimental validation of a cfd based erosion prediction procedure for jet impingement geometry. *Wear: an International Journal on the Science and Technology of Friction, Lubrication and Wear*, 394-395, 11-19.

Zolfagharnasab, M. H., M. Salimi, H. Zolfagharnasab, H. Alimoradi and C. Aghanajafi (2020). A novel numerical investigation of erosion wear over various 90-degree elbow duct sections. *Powder Technology*, 380(11), 1-3.